Transient Process Simulation of Heat Transfer in Laser Beam Welding with an Equivalent Heat Source

A. Artinov*, M. Bachmann , M. Rethmeier
BAM Federal Institute for Materials Research and Testing, Welding Technology
*Corresponding author: Unter den Eichen 87, 12205 Berlin, antoni.artinov@bam.de

Abstract

This paper presents a multiphysics modelling framework developed for the prediction of the three-dimensional transient temperature field of the laser welding process. The numerical model consists of two studies. In the first study, a steady-state CFD process simulation of full-penetration keyhole laser beam welding was performed. Considering the effects of, thermo-capillary and natural convection, latent heat of fusion and temperature-dependent material properties up to evaporation temperature the local weld pool geometry and temperature field were obtained. These results were used in the second subsequent study as an equivalent volumetric heat source by the prediction of the transient thermal cycle during and after fusion welding. Here the energy input and the movement of the heat source were realized by a novel technique, making use of pointwise constraints and a moving mesh provided with helper lines and additional remeshing condition. The numerically calculated results were compared to experimentally observed weld pool shapes and time-temperature curves showing a very good agreement.

Keywords: high power laser beam welding, transient heat transfer, equivalent volumetric heat source, moving mesh, pointwise constraints

1. Introduction

In recent years, the number of the possible industrial applications of the laser deep penetration welding has grown significantly. Due to the available laser power of up to 100 kW for solid state lasers, a single pass welding of steel plates with a thickness of up to 50 mm was made possible [1, 2]. Thus, the laser beam welding could be used by the fabrication of crane construction, shipbuilding, high pressure and vacuum vessels and much more. The advantages of the laser beam welding in contrast to the conventional multi-pass arc welding methods, in particular, the low heat input and the high reachable welding speeds, are mainly responsible for the extension of its application range. The deep penetration welding is enabled by the use of high power laser beams and the formation of the so-called keyhole [3]. This narrow and deep vapor cavity is formed by the vaporization of the molten metal allowing higher energy absorption and deeper penetration. A schematic bead-on-plate laser beam welding process is shown in Figure 1. The complex physics behind the laser-material interaction makes the understanding of the laser process and the setting of the relevant process parameters very challenging. For this reason, numerical tools, such as the Finite-Element-Method (FEM) have been used to estimate the major effects and consequences, such as melt pool geometry and temperature profile, of the laser welding process. The influence of the temperature distribution on the metallurgical changes and the thermal expansion makes it the most important factor, defining the final material properties, residual stresses and distortions of the specimen. Thus, the prediction of the transient thermal cycle is an essential part of the solution of any technically demanding joining task. There are two standard methods for the numerical description of the heat transfer. The more common and practical one is the heat source model. The energy input here is controlled by adapting a certain set of parameters to achieve good agreement between experimental and numerical results. The other, more sophisticated method, the so-called self-consistent model, considers the most important physical phenomena responsible for the heat transfer. Thus the calibration effort is minimized.

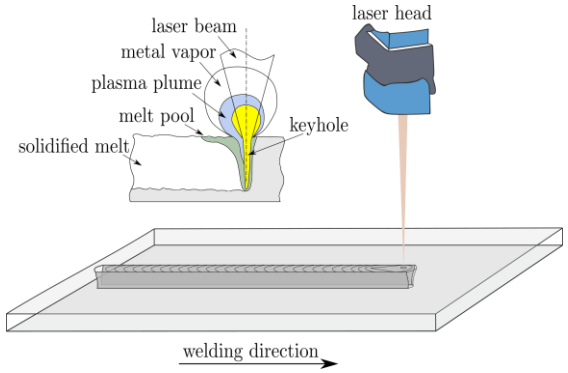

Figure 1. Schematic bead-on-plate laser beam welding process according to [4]

The earliest fundamental numerical work investigating the heat transfer by a simple analytical moving point heat source can be followed back to the early 1940s [5]. Modern heat source models such as the three-dimensional conical Gaussian and the Goldak double ellipsoidal heat source are currently used in the laser welding simulation for a realistic and accurate prediction of the thermal cycle [6, 7]. An advantage of this kind of modelling is the possible combination of the various heat sources, which allows to perfectly match the experimental results. At the other hand, the number of calibration parameters grows with any arbitrary combination of different heat sources and leads also to an increase in the calibration expense and computation time [8].

The main difficulties here are the choice of the heat source and the calibration of the corresponding parameters, which leads to the concept of the equivalent heat source approach. The equivalent heat source is defined by the melt pool geometry. This can be obtained from a thermodynamical simulation and calibrated with an additional experimental weld. In [9] a two-dimensional model with an equivalent heat source which is moved through the cross sectional model of the joint can be found. In both cases of modelling with a heat source model, the impact of some phenomena, such as vaporization, on the heat transfer is missing.

At present, due to the steadily rising computer performance, self-consistent numerical simulations, considering not only the effects of the heat transfer and the fluid flow, but also these of the energy absorption, laser reflection, and vaporization, have been performed. The coupling of these phenomena makes the description of the self-consistent keyhole evolution possible and gives researchers and engineers a better understanding of the deep penetration keyhole laser welding [10, 11]. Besides that, the evaluation of the results obtained with such models is limited through the complex interactions of the considered physical aspects making their interpretation ambiguous. This kind of modelling is more time consuming and requires large computational resources. Thus and through its complexity, this simulation method remains challenging.

This paper presents a modelling framework used to obtain an equivalent volumetric heat source and calculate the three-dimensional transient thermal cycle of the laser beam welding process. It has the advantage to predict a very accurate equivalent heat source in an admissible computing time of fewer than 24 hours by maintaining the physical reasons needed to predict the temperature distribution of the specimen. The model is calibrated by adapting the geometry of the keyhole, which is the single calibration parameter needed. It takes into account the most important physical phenomena, such as Marangoni convection at the upper and lower weld pool surfaces, natural convection due to the density variations, latent heat of the solid-liquid phase transition and temperature-dependent material properties up to evaporation temperature. The equivalent volumetric heat source is calculated and calibrated in a steady-state CFD (Computational Fluid Dynamics) simulation and thereafter used to obtain the thermal history of the part. The numerical model allows an accurate determination of both the stationary and the transient temperature distribution in and around the melt pool. The calculated numerical results show good correlation with the experimentally obtained melt pool shapes and time-temperature curves.

2. Numerical Model

The numerical modeling with COMSOL Multiphysics was divided into two steps. The first study step was the steady-state CFD simulation of the weld pool. The dependent variables for the fluid flow and the temperature field were computed with the Non-Isothermal Flow Interface (NITF). The computational domain of the CFD study was placed inside the domain of the second study. The geometry and the computational meshes can be seen in Figure 2. In the second study step, the Heat Transfer in Solids Interface (HT) was used for the prediction of the transient thermal cycle.

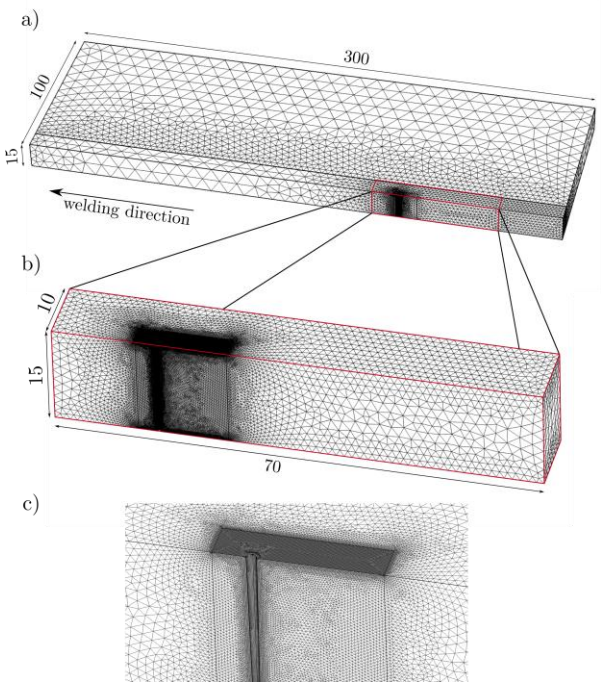

Figure 2. Geometry and meshing of the computational domains. a) represents the HT domain, b) the CFD domain and c) the enlarged vicinity of the fixed keyhole geometry

Table 1. Material properties used in the simulation [12-14]

Material property	Symbol	Value	Unit
Melting temperature	T_{melt}	1800	K
Melting interval	$T_{\mathrm{melt}} \pm \delta T$	1800 ± 35	K
Evaporation temperature	T_{evap}	3100	K
Latent heat of fusion	H_{f}	$2.47 \cdot 10^{5}$	$\mathrm{J\,kg^{-1}}$
Marangoni coefficient	$\partial\gamma/\partial T$	$-4.3 \cdot 10^{-4}$	$\mathrm{N\,m^{-1}\,K^{-1}}$
Coefficient of thermal Expansion	β	$1.5 \cdot 10^{-5}$	$\mathrm{K^{-1}}$
Heat transfer coefficient (air)	h	15	$\mathrm{W\,m^{-2}\,K^{-1}}$
Material properties at T_{melt}			
Mass density	ρ	7850	$\mathrm{kg\,m^{-3}}$
Dynamic viscosity	η	$6.2 \cdot 10^{-3}$	$\mathrm{Pa \cdot s}$
Thermal conductivity	λ	32	$\mathrm{W\,m^{-1}\,K^{-1}}$
Heat capacity	c_{p}	707	$\mathrm{J\,kg^{-1}\,K^{-1}}$
Apparent heat capacity	$c_{\mathrm{p}}^{\mathrm{app}}$	4618	$\mathrm{J\,kg^{-1}\,K^{-1}}$

A pointwise constraint was applied to the nodes belonging to the CFD domain to prescribe their temperatures with the corresponding temperatures calculated in the first study step. After that the CFD domain was moved through the specimen by a moving mesh approach, making use of the Deformed Geometry Interface. Additionally, helper lines and an automatic remeshing option were added to provide better deformation of the mesh. By known deformation at the ends of the helper lines, the Laplace's equation was solved giving the deformation of the nodes along these lines. Thus a smoother mesh deformation was achieved. The Laplace's equation was implemented via the Coefficient Form Edge PDE (Partial Differential Equation) and the Coefficient Form Boundary PDE from the PDE Interface. Both domains represents just one-half of the real part to be modelled, exploiting the symmetry along the weld. For the discretization of the computational domains tetrahedral and triangular elements were used. The CFD domain was discretized by 1.5 millions linear finite elements and the HT domain by about 10^5. An element increase of about 10% after the remeshing was noticed. The degrees of freedom could be limited to around 2 millions in the CFD simulation. Here the dependent variables were separated and solved in segregated groups with the less memory intensive iterative multigrid approach. The visualization of the dependent variables and the coupling between the single physics is shown in Figure 3, where **u**, T, λ, $C_{\mathrm{p}}, \rho, \gamma$ and μ are the flow velocity, temperature, thermal conductivity, heat capacity, mass density, surface tensions and dynamic viscosity respectively. The temperature dependent material properties used in the model are summarized in Table 1. Figure 4 visualizes the thermo-physical properties normalized by the corresponding values of the variables at the melting temperature. The set-up of the segregated solver can be seen in the flowchart of the multi-physics modelling framework in Figure 5.

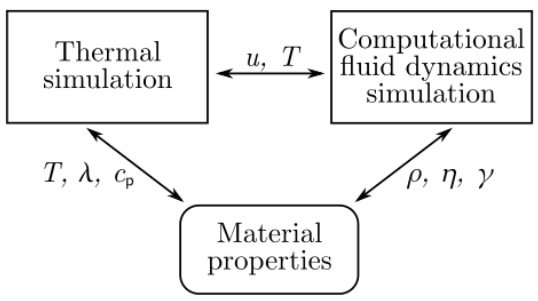

Figure 3. Interactions between the single physics

2.1 Assumptions

For numerical reasons and time efficiency the problem statement was simplified and contains only the most important physical aspects of the fluid flow and the heat transfer.

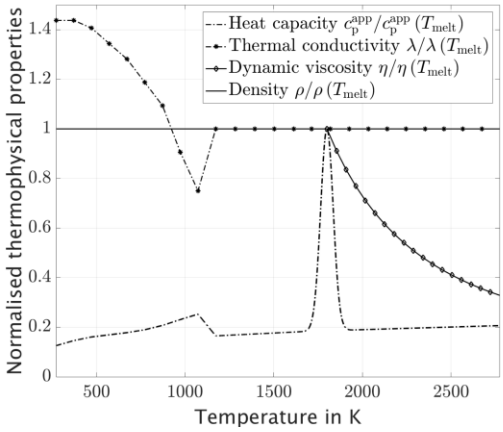

Figure 4. Thermo-physical properties used in the model taken from [12-14]

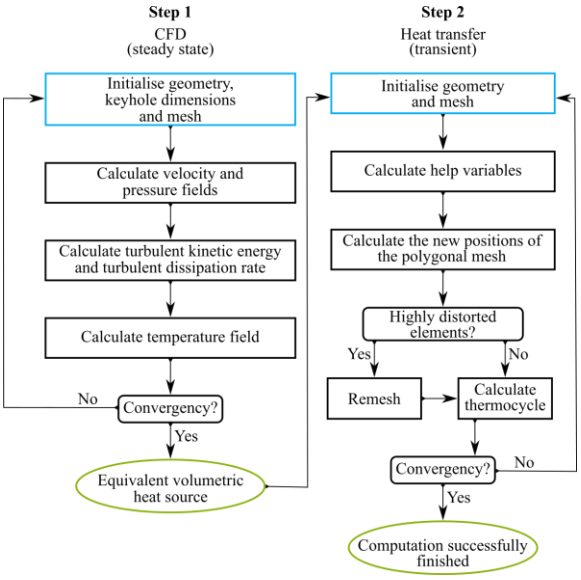

Figure 5. Flowchart of the multi-physics simulation

The basic assumptions are given as follows:

- Steady-state approach
- Fixed free surface and keyhole geometries
- Adapted size of the CFD domain to fulfil the adiabatic boundary condition on the rear wall, see Figure 6
- A turbulent flow pattern, described by the Reynolds-averaged Navier-Stokes (RANS) equations with the standard $\kappa - \varepsilon$ model
- Density deviations were modelled by the Boussinesq approximation [15]
- Latent heat of the solid-liquid phase change was modelled with the apparent heat capacity method [16]
- Solidification was modelled by the Carman-Kozeny equations [17]

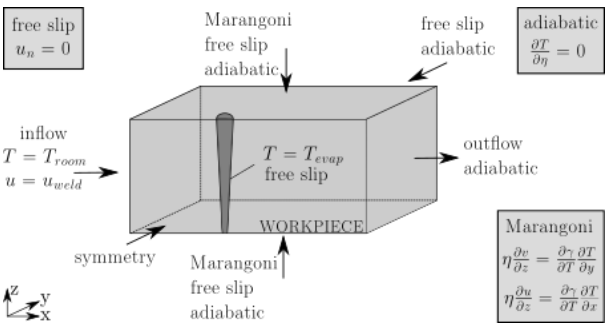

Figure 6. Boundary conditions for the CFD simulation

2.2 Governing Equations

The governing equations representing the conservation of mass, momentum and energy as well the equations of the turbulence model used for the description of the problem were taken as they are implemented in the commercial finite element software COMSOL Multiphysics. In the following, the modifications and extensions applied in the model will be given.

- The source term **F** in the momentum conservation reads:

$$\mathbf{F} = \rho \mathbf{g} \beta (T - T_{\text{melt}}) - c_1 \frac{(1 - f_{\text{L}})^2}{f_{\text{L}}^3 + c_2} (\mathbf{u} - \mathbf{u_{weld}}).$$

This equation takes into account the buoyancy force (first term) and describes the solidification behavior of the melt (second term). Here β and $\mathbf{g}$ are the coefficient of thermal expansion and the gravitational constant. c_1 and c_2 are computational constants and f_{L} denotes the liquid fraction. The liquid fraction was defined as a piecewise function:

$$f_{\text{L}} = \begin{cases} 0 & T < T_{\text{sol}} \\ \dfrac{T - T_{\text{sol}}}{T_{\text{liq}} - T_{\text{sol}}} & T_{\text{sol}} \leq T \leq T_{\text{liq}}. \\ 1 & T > T_{\text{liq}} \end{cases}$$

- The Kays-Crawford heat transfer turbulence model was used to account for the turbulent heat conductivity.

- The latent heat of fusion was modelled by the apparent heat capacity method as follows:

$$C_{\text{p}}^{\text{app}} = C_{\text{p}}^{0} + \frac{\exp\left[-\left(\frac{T - T_{\text{melt}}}{\delta T}\right)^2\right]}{\sqrt{\pi}\delta T} \cdot H_{\text{f}}.$$

Here $\delta T = 35$ K is the temperature range within the amount of latent heat H_{f} is uniformly released.

- The displacement of the helper lines was calculated with the Laplace's equation:

$$\frac{\partial^2\left(\frac{\partial x_i}{\partial t}\right)}{\partial X^2} + \frac{\partial^2\left(\frac{\partial x_i}{\partial t}\right)}{\partial Y^2} + \frac{\partial^2\left(\frac{\partial x_i}{\partial t}\right)}{\partial Z^2} = 0.$$

The uppercase X, Y and Z represent here the original positions of the helper lines, x, y and z the positions after deformation and $x_i = (x, y, z)$.

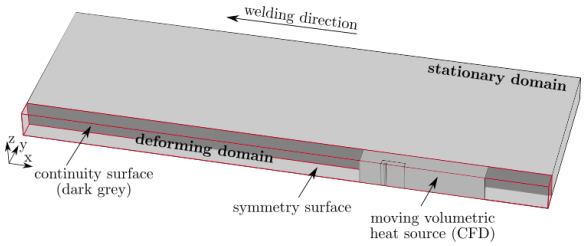

Figure 7. Boundary conditions for the HT simulation

2.3 Boundary conditions

The boundary conditions used in the CFD simulation can be taken from Figure 6. They were also used in similar studies, see [18, 19]. Here the energy input was assured by setting the temperature of the keyhole surface to the evaporation temperature of the material. The keyhole was chosen to be a right circular cone with a top radius of 0.41 mm and a bottom radius of 0.26 mm and was excluded from the geometry. The free slip condition on the keyhole surface and on the upper and lower side of the part prevented a fluid flow in the normal direction. On the upper and lower surface of the plate, a Marangoni boundary condition was applied to consider the fluid flow due to the temperature-dependent surface tension. The welding speed was set to 2 m min^{-1} and room temperature was assumed at the inlet. In Figure 7 the boundary conditions for the transient HT simulation can be seen. A heat flux q_0 between the exterior surfaces and the ambient air was assumed:

$$-n \cdot (-\lambda \nabla T) = q_0,$$

where $q_0 = h(T_0 - T)$ W m^{-2} and h (heat transfer coefficient) of 15 W m^{-2} K^{-1}. A continuity boundary condition was applied to ensure a smooth heat transition between the stationary (destination domain) and the deforming domain (source domain):

$$-n_{\mathrm{dst}} \cdot (\lambda \nabla T)_{\mathrm{dst}} = n_{\mathrm{src}} \cdot (\lambda \nabla T)_{\mathrm{src}}$$
$$T_{\mathrm{dst}} = T_{\mathrm{src}} \cdot$$

In both simulations the symmetry plane was set to adiabatic so that no heat flux in normal direction was allowed.

3. Experimental set up

For the validation and the calibration of the numerical results temperature measurements have been done. The positions of the measurements of the temperature can be seen in Figure 8. The positions of the thermocouples on the bottom side were similar to these on the upper side of the plate. The specimen

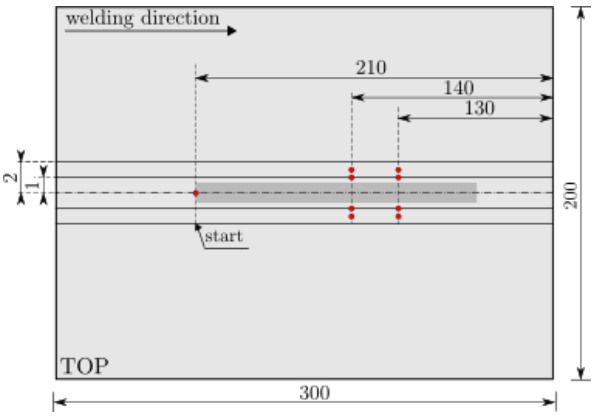

Figure 8. Positions of the measurements of the temperature

thickness was 15 mm. A weld with a length of about 165 mm was produced. The welding process was performed with a low alloyed steel and laser power of 18 kW.

4. Results

The prediction of an appropriate equivalent heat source was the main goal of the present investigation. For this the obtained three-dimensional weld pool geometry has to be as accurately as possible. The weld pool shape is strongly influenced by the Marangoni convection on the weld at the upper and lower weld pool boundaries. This effect divides the weld pool shape into three regions, the lower, middle and upper region. Due to the temperature decrease along the weld pool an increase of the surface tension on the free surfaces of the upper and lower regions is experienced. This causes the two vortexes, which transport the melt away from the keyhole surface to the edge of the weld pool and form the shape of the upper and lower region. The effect of the thermocapillary convection can be seen in the symmetry plane of the CFD simulation in Figure 9.

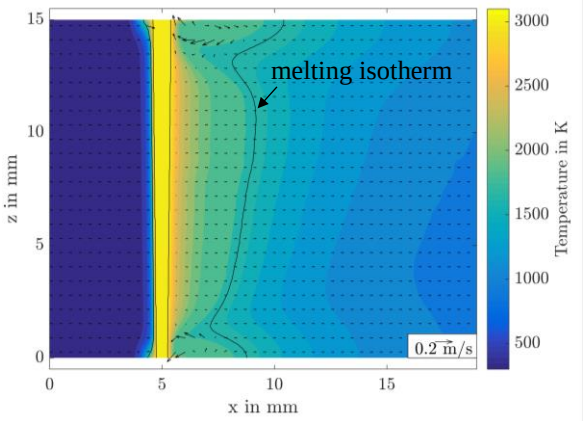

Figure 9. Temperature and velocity field in the symmetry plane of the CFD simulation

The smaller dimensions of the vortex on the lower side can be explained by the reduced energy input through the conical structure of the keyhole. The effects of the natural convection modelled by the Boussinesq approximation are noticeable in the velocity field but neither of the implemented physical aspects seems to be strong enough to influence the fluid flow in the middle region. Here the shape of the region is defined by the geometry of the keyhole and the welding speed. Note also the wake space behind the keyhole caused by the flow of the melt around it. For the validation of the computed results, the weld pool length defined by the black curve (the melting isotherm) in Figure 9 was compared to the length of the end crater from the experiments. The numerically obtained values of about 6.3 mm on the upper and 4.4 mm on the lower side agreed very well with the experimental results.

As next the cross sections were compared. First, a range for the experimental data was generated. For this all four metallographic cross sections along the weld were compared to each other. The broadest and the narrowest cross sections were used to define the range of the experiments. The simulated cross section was obtained as a projection of the melt pool defined by the melting temperature. A metallographic cross section and the comparison between the numerical and experimental results can be seen in Figure 10. The observed simulated cross section lies in the range of the experimental data and follows their shape. Herewith the validation of the dimensions of the three-dimensional melt pool is finalized so that this can be used as an equivalent volumetric heat source in the transient HT simulation. The effects of convection do not have to be considered in the HT simulation once this is done in the CFD model. The HT model takes into account heat conduction as the single physical phenomena responsible for the heat transfer. By prescribing the nodes temperatures within the CFD domain and moving this through the plate the energy input was assured. Figure 11 shows the temperature distribution at different times. Noticeable here is the constant temperature field in the prescribed region during the process. The experimentally observed time-temperature curves, measured at different distances from the weld centerline are compared

Figure 10. Metallographic cross section a) and comparison of experimental and numerical results b)

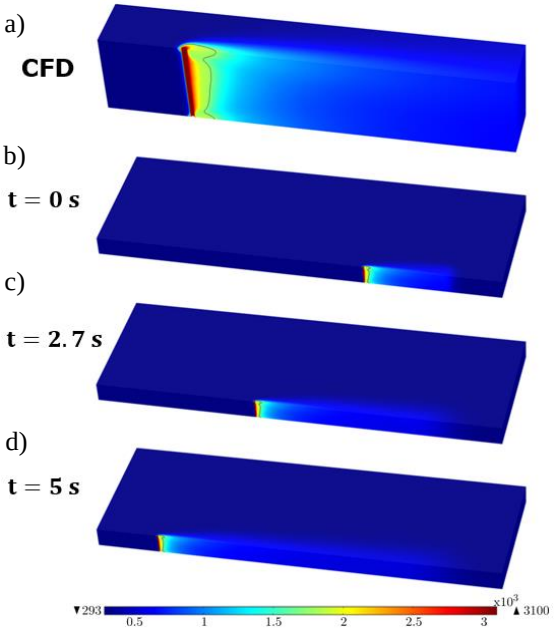

Figure 11. a) shows the temperature field obtained in the CFD simulation. b), c) and d) show the temperature field during the process at different times

to the simulated time-temperature curves in Figure 12. Hence the relation between the measured maximum temperature and the distance of the thermocouple element from the weld centerline is obtained. As expected an increase in the distance leads to a decrease of the maximum measured temperature on both upper and lower side. Note here that the width of the weld pool on the lower side is smaller. This is caused by the linear decrease of the keyhole radii from the top to the bottom. Thus the differences in the maximum temperature measured on the lower side by a distance of 1.13 mm and on the upper side by a distance of 1.52 mm is trustworthy. The investigation of the numerical and experimental data has shown that the modelling framework is able to predict the behavior of the thermal cycle very well.

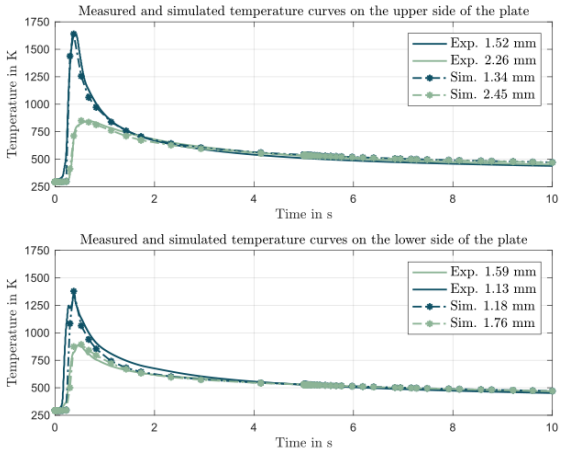

Figure 12. Measured and simulated temperature curves

Conclusions

In the present work a modelling framework for the calculation of a reliable equivalent heat source, defined through the obtained weld pool geometry, and the prediction of the thermal behavior during fusion welding has been established. It combines the advantages of the standard modelling methods and reduces both the number of physical aspects to be considered and the number of calibration parameters. Thus the simulation time (computational time plus the time for the calibration effort) was reduced to less than one day. Due to the considered effects of Marangoni- and natural convection, latent heat of fusion and metallurgical phase changes the information of the fluid flow and its influence on the resulting local temperature field and consequently on the transient thermal cycle was conserved. The obtained thermal cycle would allow the coupling of thermomechanical and process simulation and the further investigation of the complex interactions between fluid flow and local stress and strain fields.

Acknowledgements

Funded by the Deutsche Forschungsgemeinschaft (German Research Foundation) - BA 5555/1-1.

References

1. Bachmann, M., Gumenyuk, A., & Rethmeier, M. (2016). Welding with high-power lasers: trends and developments. Physics Procedia, 83, 15-25.
2. Zhang, X., Ashida, E., Tarasawa, S., Anma, Y., Okada, M., Katayama, S., & Mitzutani, M. (2011). Welding of thick stainless steel plates up to 50 mm with high brightness lasers. Journal of Laser Applications, 23(2), 022002.
3. Ready, J. F., & Farson, D. F. (Eds.). (2001). LIA handbook of laser materials processing. Orlando: Laser Institute of America.
4. Dilthey, U. (2006). Schweißtechnisches Fertigungsverfahren 1 – Schweiß- und Schneid-technologien. (3. Aufl.). Berlin Heidelberg: Springer-Verlag, 179.
5. Rosenthal, D. (1946). The Theory of Moving Sources of Heat and Its Application of Metal Treatments. Transactions of ASME, 68, 849-866.
6. Balasubramanian, K. R., Siva Shanmugam, N., Buvanashekaran, G., & Sankaranarayanasamy, K. (2008). Numerical and experimental investigation of laser beam welding of AISI 304 stainless steel sheet. Adv. Produc. Engineer. Manag, 3(2), 93-105.
7. Goldak, J., Chakravarti, A., & Bibby, M. (1984). A new finite element model for welding heat sources. Metallurgical and Materials Transactions B, 15(2), 299-305.
8. Chukkan, J. R., Vasudevan, M., Muthukumaran, S., Kumar, R. R., &Chandrasekhar, N. (2015). Simulation of laser butt welding of AISI 316L stainless steel sheet using various heat sources and experimental validation. Journal of Materials Processing Technology, 219, 48-59.
9. Radaj, D., Häuser, H., & Braun, S. (1998). Numerische Simulation von Eigenspannungen und Verzug bei Schweißverbindungen aus AlMgSi-Legierungen. Konstruktion, 50(7-8), 31-37.
10. Gaied, S., Courtois, M., Carin, M., & Le Masson, P. (2015). Optimization of Welding Parameters using 3D Heat and Fluid Flow Modeling of Keyhole Laser Welding. Proceedings of the COMSOL Conference, Grenoble, France.
11. Ai, Y., Jiang, P., Shao, X., Li, P., & Wang, C. (2017). A three-dimensional numerical simulation model for weld characteristics analysis in fiber laser keyhole welding. International Journal of Heat and Mass Transfer, 108, 614-626.
12. Hildebrand, J. (2008). Numerische Schweiß-simulation-Bestimmung von Temperatur, Gefüge und Eigenspannung an Schweißverbindungen aus Stahl- und Glaswerkstoffen.
13. Sahoo, P., DebRoy, T., & McNallan, M. J. (1988). Surface tension of binary metal-surface active solute systems under conditions relevant to welding metallurgy. Metallurgical and Materials Transactions B, 19(3), 483-491.
14. Mills, K. C. (2002). Recommended values of thermophysical properties for selected commercial alloys. Woodhead Publishing.
15. Faber, T. E. (1995). Fluid dynamics for physicists. Cambridge University Press.
16. Hashemi, H. T., & Sliepcevich, C. M. (1967). A numerical method for solving two-dimensional problems of heat conduction with change of phase. In Chem. Eng. Prog. Symp. Series (Vol. 63, No. 79, pp. 34-41).
17. Brent, A. D., Voller, V. R., & Reid, K. T. J. (1988). Enthalpy-porosity technique for modeling convection-diffusion phase change: application to the melting of a pure metal. Numerical Heat Transfer, Part A Applications, 13(3), 297-318.
18. Bachmann, M., Gumenyuk, A., & Rethmeier, M. (2011). Multiphysics Process Simulation of the Electromagnetic-Supported Laser Beam Welding. Proceedings of the COMSOL Conference, Stuttgart, Germany.
19. Bachmann, M., Gumenyuk, A., & Rethmeier, M. (2012). Multi-Physics Process Simulation of Static Magnetic Fields in High Power Laser Beam Welding of Aluminum. Proceedings of the COMSOL Conference, Milan, Italy.